$$a^{\ell}_{AlO_{1.5}} = \frac{X_{AlO_{1.5}} - (X_{NaO_{0.5}} + X_{KO_{0.5}})}{\Sigma NM}$$

$$a^{\ell}_{SiO_2} = \frac{X_{SiO_2}}{\Sigma NF} \quad a^{\ell}_{CaO} = \frac{X_{CaO}}{\Sigma NM} \qquad (7.34)$$

where ΣNM is the sum of the "network modifiers" and ΣNF is the sum of the "network formers":

$$\Sigma NM = X_{AlO_{1.5}} + X_{CaO} + X_{MgO} + X_{FeO} + X_{P_2O_5} + X_{TiO_2} + X_{MnO} + X_{CrO_{1.5}} - X_{NaO_{0.5}} - X_{KO_{0.5}} \qquad (7.35)$$

$$\Sigma NF = X_{SiO_2} + X_{NaO_{0.5}} + X_{KO_{0.5}} \qquad (7.36)$$

The activities of Sc, Y, and the rare earths are assumed equal to:

$$a^{\ell}_i = \frac{X^{\ell}_i}{\Sigma NM} \quad a^{cpx}_i = X^{cpx}_i \qquad (7.37)$$

where i is Sc, Y, La, and so on.

How does the D* we defined above relate to D as defined in eqn. 7.2? With activities as defined in eqn. 7.34, D is related to D* as:

$$D_i = D^*_i \frac{\sum moles\ oxides\ cpx \times Mol.\ Wt.\ i}{\sum NM \sum moles\ oxides\ liq. \times Mol.\ Wt.\ i} \qquad (7.38)$$

The molecular weight terms cancel, of course, and the molar sums for cpx and basaltic liquid will generally be equal to within about 5%, so that eqn. 7.38 simplifies to:

$$D_i \approx \frac{D^*_i}{\Sigma NM} \qquad (7.39)$$

Example 7.2 illustrates this calculation.

Hack *et al.* (1994) extended the work of Gallahan and Nielsen (1992) to include the effects of pressure. They found the equilibrium constant for reaction 7.26 could be expressed as follows:

$$\ln K = c_1 + c_2 \times \frac{10000}{T} + \frac{c_3}{P} + c_4 X^{cpx}_{Ca} c_5 D^{cpx/\ell}_{Ti} + c_6(Al + Si - Na - K)$$

where T is temperature (in kelvin), P is pressure (in kbar), X_{Ca} is the mole fraction of clinopyroxene octahedral sites occupied by Ca, D_{Ti} is the clinopyroxene–melt partition coefficient for Ti, (Al + Si − Na − K) refers to the mole fraction of the corresponding oxides in the melt, and $c_1 \ldots c_6$ are regression coefficients. This equation is considerably more complex than eqn. 7.30, but is only marginally more accurate. It does have the advantage of including the pressure term.

Beattie (1993) used a modification of the two-lattice model to predict the partitioning

Example 7.2 Calculating partition coefficients

Using the composition of the basalts given below, calculate the clinopyroxene-matrix partition coefficients for La and Sm using the Gallahan and Nielsen equations and the coefficients given in Table 7.4. Assume a temperature of 1080°C.

Oxide	Mauna Loa tholeiite wt %	Mount Hope alkali basalt wt %
SiO_2	49.56	50.95
TiO_2	4.28	1.38
Al_2O_3	14.09	17.87
FeO	12.47	8.64
MnO	0.22	0.21
MgO	4.62	6.18
CaO	9.63	11.29
Na_2O	3.03	2.32
K_2O	1.18	0.95
P_2O_5	1.02	0.51

(*Continued*)

Answer: Once again this is a problem that is best done in a spreadsheet. Our first task will be to convert the wt. percent to mole fractions. We calculate the moles of each component (Gallahan and Nielsen chose their components as single cation oxides, except for P_2O_5) by dividing by the molecular weight. We convert this to mole fractions by dividing by the sum of the moles of all components. Then we calculate the sums of the network formers and network modifiers (eqns. 7.33 and 7.36), and finally the activities of SiO_2 and $AlO_{1.5}$ using eqn. 7.34. We calculate K using eqn. 7.28 (temperature in kelvins, as in all thermodynamically based formulae). The distribution coefficient, D*, can then be calculated using eqn. 7.31. Finally, we convert to D using eqn. 7.39.

Though the temperature is the same and the compositions of these basalt magmas are similar, there is a large difference, almost a factor of 2, in the partition coefficients we have calculated.

	Mauna Loa			Mt. Hope			
Oxide	**wt %**	**moles**	**mol fract.**	**wt %**	**moles**	**mol fract.**	**Mole. Wt**
SiO2	49.56	0.826	0.472288	50.95	0.8492	0.473491	60
TiO2	4.28	0.054	0.030636	1.38	0.0173	0.009633	79.88
Al2O3	14.09	0.276	0.158029	17.87	0.3505	0.195454	50.98
FeO	12.47	0.174	0.099235	8.64	0.1203	0.067051	71.85
MnO	0.22	0.003	0.001773	0.21	0.003	0.001651	70.94
MgO	4.62	0.115	0.065532	6.18	0.1533	0.085486	40.31
CaO	9.63	0.172	0.098185	11.29	0.2013	0.112255	56.08
Na2O	3.03	0.098	0.055887	2.32	0.0748	0.04173	31
K2O	1.18	0.025	0.014325	0.95	0.0202	0.011247	47.1
P2O5	1.02	0.007	0.004109	0.51	0.0036	0.002003	141.94
Total	100.1	1.749	1	100.3	1.7934	1	
NM			0.387289			0.420556	
NF			0.5425			0.526468	
aSiO2			0.870578			0.899374	
aAlO1.5			0.065156			0.126982	
ln(aSiO2*aAlO1.5)			–2.86958			–2.16977	
T	1353						
	La	Sm	Mauna Loa			Mount Hope	
a	119	11371	lnD La	lnD Sm		lnD La	lnD Sm
b	1.95	8.6	–4.73162	–3.0653		–4.03182	–2.3655
ln K	–1.86205	–0.1957	D* La	D* Sm		D* La	D* Sm
D*			0.008812	0.0466		0.017742	0.0939
D			**0.02275**	**0.1204**		**0.04219**	**0.223329**

of Mg, Fe, Mn, Co, and Ni between olivine, orthopyroxene, and melt as a function of temperature and composition. Beattie relaxes the assumption that the network-forming lattice is ideal and introduces an empirical function to calculate the activity of SiO_2. He then calculated values of $\Delta H_{m'}$ $\Delta V_{m'}$ and ΔS_m from experiments on mineral melt pairs. The resulting thermodynamic data were used to calculate the equilibrium constant for the exchange reaction, for example:

$$2MO^{\ell} + Mg_2SiO_4^{ol} \rightleftharpoons 2MgO^{\ell} + M_2SiO_4^{ol}$$

where M is Fe, Mn, Co, and so on. The equilibrium constant is:

$$K = \left(\frac{D_M^{\alpha/\ell}\lambda_{MO}^{\alpha}\lambda_{MgO}^{\ell}}{D_{Mg}^{\alpha/\ell}\lambda_{MgO}^{\alpha}\lambda_{MO}^{\ell}}\right)^2 \exp\left(\frac{\Delta S}{R} - \frac{\Delta H + (P - P^{\circ})\Delta V}{RT}\right) \quad (7.40)$$

where γ is the activity coefficient, and ΔS, ΔH, and ΔV refer to the difference in entropy, enthalpy, and volume changes of fusion between the Mg version and the M version of phase α (e.g., $\Delta S = \Delta S_m^{M\text{-}\alpha} - \Delta S_m^{MgO\text{–}\alpha}$).

7.4.4 Mineral–liquid partition coefficients for mafic and ultramafic systems

As we have seen, partition coefficients depend on temperature, pressure, and the composition of the phases involved. There are nevertheless circumstances when a general set of partition coefficients is useful. For example, temperature or melt composition may not be known, or great accuracy may not be needed. Table 7.5 is a set of mineral–melt partition coefficients for mafic and ultramafic magmas. They have been primarily assembled from the GERM partition coefficient database (www.earthref.org/GERM) and adjusted where necessary to make them self-consistent. The uncertainties in some cases can be considerable. This is particularly true where the values are very small, in which case the uncertainty may be an order of magnitude or more (in most modeling efforts, however, once the value of a partition coefficient is less than

Table 7.5 Mineral–melt partition coefficients for basalts.

	Olivine	Opx	Cpx	Plag	Spinel	Garnet	Amph
Li	0.35	0.11	0.25	0.3	0.13	0.04	0.1
Be	0.03	0.06	0.05	0.37	0.1	0.004	0.15
B	0.01	0.003	0.03	0.13	0.08	0.005	0.06
K	0.001	0.003	0.007	0.15		0.05	1.4
Sc	0.3	0.6	2	0.08	0.5	2.6	2.1
V	0.09	2.6	0.78	0.1	1.3	3.5	4.0
Ga	0.024	0.38	0.7	1.7	3	1.0	0.5
Ge	1.0	1.4	2	0.5	0.1	0.5	0.3
Rb	0.0001	0.001	0.005	0.1	0.03	0.007	0.5
Sr	0.0001	0.001	0.1	1.5	0.005	0.01	0.3
Y	0.005	0.01	0.4	0.008	0.05	3.1	0.4
Zr	0.001	0.004	0.12	0.03	0.06	0.27	0.2
Nb	0.0001	0.015	0.01	0.1	0.0006	0.05	0.15
Cs	0.0002	0.0009	0.06	0.05	~0	0.0005	0.06
Ba	0.000002	0.000002	0.0005	0.3	0.0006	0.0007	0.28
La	0.000001	0.0007	0.07	0.08	0.001	0.001	0.04
Ce	0.000003	0.0017	0.12	0.06	0.0015	0.005	0.1
Pr	0.00001	0.003	0.18	0.05	0.0023	0.02	0.17
Nd	0.00004	0.006	0.28	0.05	0.0034	0.07	0.21
Sm	0.0001	0.012	0.42	0.05	0.005	0.2	0.25
Eu	0.0005	0.024	0.45	0.5	0.006	0.4	0.33
Gd	0.002	0.04	0.49	0.04	0.0065	0.6	0.36
Tb	0.005	0.06	0.56	0.04	0.007	1.0	0.4
Dy	0.009	0.08	0.62	0.045	0.0071	1.7	0.46
Ho	0.013	0.1	0.66	0.05	0.0072	2.5	0.51
Er	0.015	0.13	0.72	0.055	0.0073	3.6	0.57
Tm	0.018	0.025	0.76	0.058	0.0074	5.0	0.585
Yb	0.02	0.02	0.8	0.06	0.0075	6.5	0.6
Lu	0.022	0.22	0.8	0.06	0.0075	7.1	0.6
Hf	0.001	0.021	0.24	0.03	0.05	0.2	0.6
Ta	0.00001	0.015	0.01	0.17	0.06	0.1	0.1
Pb	0.0001	0.0001	0.001	0.75	0.0005	0.0001	0.05
Th	0.00001	0.006	0.0013	0.13	0.01	0.001	0.004
U	0.00001	0.015	0.0001	0.1	0.01	0.01	0.004

Based on values in the GERM partition coefficient database (http://earthref.org/GERM/). Some values were interpolated; others were adjusted for self-consistency.

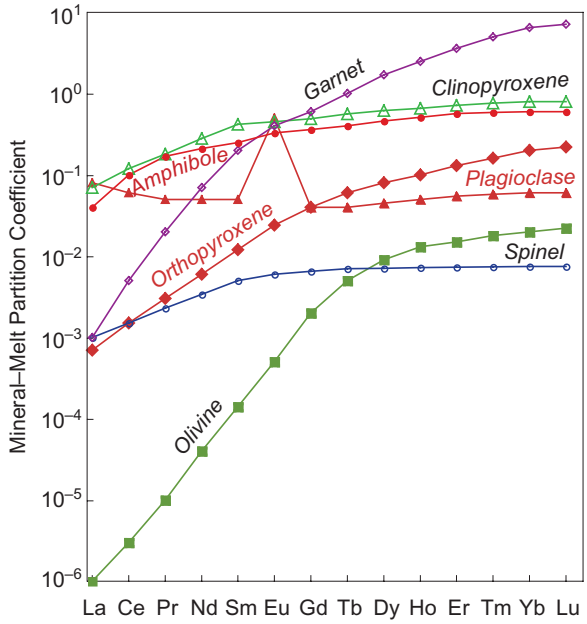

Figure 7.16 Rare earth mineral–melt partition coefficients for mafic magmas. Data from Table 7.5.

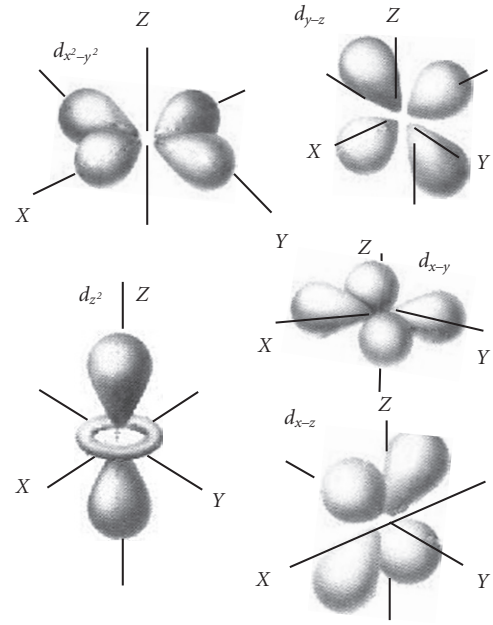

Figure 7.17 Geometry of the *d* orbitals.

about 0.01, its exact value will make very little difference). Uncertainties of partition coefficient values close to 1 are much smaller.

Figure 7.16 illustrates the rare earth partition coefficients from this dataset. In general, the minerals clinopyroxene, garnet and plagioclase and, when present, amphibole (amphibole is not usually present in basalts because it is not stable at low pressure or above 1100°C) will control the patterns of incompatible element partitioning during melting and crystallization of basaltic magmas because they have the highest partition coefficients. Olivine, though by far the most abundant mineral in the upper mantle, will produce little fractionation* of incompatible elements because its partition coefficients are so low. Spinel, which is usually not present in more than a few volume percent, will also have little effect on relative trace element abundances. On the other hand, olivine largely controls the fractionation of the compatible transition metals.

7.5 CRYSTAL-FIELD EFFECTS

We pointed out earlier that the ions of the alkalis, alkaline earths and rare earths can be satisfactorily modeled as hard spheres containing point charges at their centers. This model of ionic behavior is notably less satisfactory for many of the transition metals, because of the complex geometry of the bonding electron orbitals, illustrated in Figure 7.17. A more accurate prediction of bonding and substitution requires consideration of the electrostatic field of surrounding ions on the electron structure of transition elements.

Crystal-field theory, which was developed in 1929 by physicist Hans Bethe, describes the effects of electrostatic fields on the energy levels of a transition-metal ion in a crystal structure. These electrostatic forces originate from the surrounding negatively charged anions or dipolar groups, known as ligands. Crystal field theory is the simplest of several theories that attempt to describe the interaction and

* *Fractionation*, in this context, refers to a change in the relative abundances, or ratios, of elements. For example, if the ratio of La to Sm changes during a process, these elements are said to have been fractionated by that process.

bonding between ligands and transition metals. In crystal field theory, the ligands are regarded simply as negative point charges about the transition metal ion. The electromagnetic field produced by these ligands, the "crystal field", destroys the spherical symmetry possessed by an isolated transition metal. The changes induced depend upon the type, position, and symmetry of the coordinating ligands, as well as the nature of the transition metal.

In the usual case, electron orbitals are filled successively from inner to outer as one proceeds "up" the periodic table to heavier elements. In transition metals, however, filling of the outermost *s* orbital is begun before the *d* orbitals are completely filled. Ions are formed when the outermost *s* and, in some cases, some of the outermost *d* electrons (outermost will be *4s* and *3d* for the first transition series, *5s* and *4d* for the second) are removed from the metal.

In an isolated first series transition metal, the five *3d* orbitals (each containing up to 2 electrons: a total of 10 electrons are possible in the *d* orbitals) are energetically equivalent and have equal probability of being filled: they are said to be *degenerate*. They possess, however, different spatial configurations (Figure 7.17). One group, the e_g orbitals, consisting of the d_{z^2} and the $d_{x^2-y^2}$ orbitals, has lobes directed along the Cartesian coordinates, while the t_{2g} group, consisting of the d_{xy}, d_{yz}, and d_{xz}, possess lobes between the Cartesian axes. In a crystal field the *3d* orbitals are no longer degenerate, and some have lower energy than others. Thus there can be a relative energy gain by preferentially filling low-energy *d* orbitals. This energy gain is traded off against the energy cost of placing two electrons in a single orbital. Depending on this tradeoff, preferentially filling low-energy *d* orbitals can lower the overall energy of some transition metal ions, hence stabilizing them, in certain lattice configurations relative to other configurations. *The effect is a lattice site preference of some transition metals that would not be predicted simply from consideration of ion charge and size.*

In octahedral coordination, the transition metal is surrounded by six identical ligands (Figure 7.18). Electrons in all orbitals are repelled by the negatively charged ligands, but electrons in the e_g orbitals, the orbitals directed toward the ligand, are repelled to a greater extent than those in the t_{2g} orbitals. *The energy separation between the t_{2g} and the e_g orbitals is termed octahedral crystal-field splitting and is denoted by Δ_o. The t_{2g} orbitals are lowered by $^2/_5\Delta_o$ while the e_g orbitals are raised by $^3/_5\Delta_o$ relative to the mean energy of an unperturbed ion.* Therefore each electron in a t_{2g} orbital stabilizes a transition metal ion by $^2/_5\Delta_o$ and each electron in an e_g orbital diminishes stability by $^3/_5\Delta_o$. The resultant net stabilization energy (i.e., $\Sigma\Delta_o$), is called the *octahedral crystal field stabilization energy* or octahedral CFSE.

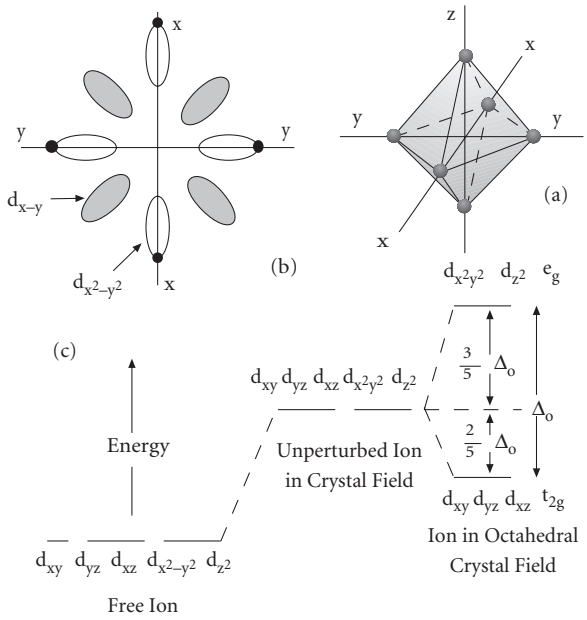

Figure 7.18 (a) Orientation of ligands and Cartesian coordinates for a metal ion in octahedral coordination. (b) Orientation of ligands (points) and d_{xy} (shaded) and $d_{x^2-y^2}$ (unshaded) orbitals in the $x - y$ plane of a metal in octahedral coordination. (c) Energy-level diagram for *d* orbitals of a free transition metal ion, an ion in a spherically symmetric crystal field and an octahedral crystal field. In an octahedral crystal field, the energy of the *d* orbitals projected between the coordinates and the ligands (the t_{2g} orbitals) are lowered relative to the energy of the orbitals projected toward the ligands (e_g orbitals). After Burns (1970). Figures 2.3 and 2.4. Reprinted with the permission of Cambridge University Press.

How electrons are distributed in an octahedrally coordinated transition metal is governed by two opposing tendencies. Coulomb forces between electrons cause them to be distributed over as many orbitals as possible, but crystal-field splitting favors the occupation of lowest energy orbitals. These two factors in turn depend upon the number of *d* electrons possessed by the metal and the strength of the crystal field.

In ions having 1, 2 or 3 *d* electrons, all electrons will be in only t_{2g} orbitals, regardless of the strength of the crystal field, since there is only one electron per orbit. In ions having 8, 9, or 10 electrons in *d* orbitals, each orbital must contain at least 1 electron and three orbitals must contain 2 electrons, so all the 3 t_{2g} orbitals will be filled even for weak ligands. But in ions having 4, 5, 6 and 7 *d* electrons, there is a choice. If the crystal-field splitting is large, as in the case of strong field ligands, all electrons are in t_{2g} orbitals. This is the *low-spin* case, because the spins of electrons are anti-aligned (recall the Pauli exclusion principle that electrons can only occupy the same orbit if their spins are opposite). When the crystal-field splitting is small, the energy cost of placing two electrons in the same orbit is greater than the energy gain from the octahedral CFSE, and electrons are distributed over both t_{2g} and e_g orbitals. This is known as the *high-spin* case because the electrons will preferentially occupy different orbitals with their spins parallel. Apart from Co^{3+} and Ni^{3+}, all first series transition metals exist in the high-spin state on the Earth's surface. Cr^{3+}, Ni^{2+}, and Co^{3+} have particularly high CFSE in octahedral coordination.

The distinction between high- and low-spin configurations is important in understanding magnetic properties of transition metal compounds because magnetism relates to spin alignment of electrons. Also, the crystal-field splitting energies are in the visible light band and hence relate to the coloration of transition-metal-bearing minerals. For example, consider titan-augite (a variety of clinopyroxene containing appreciable amounts of Ti). In Ti^{3+}, the single *d* electron is normally in the t_{2g} orbital. Absorption of light of appropriate frequency ($\nu = \Delta_o/h$) excites the electron into an e_g orbital. This energy corresponds to violet light, which is emitted when the electron returns to the t_{2g} orbital.

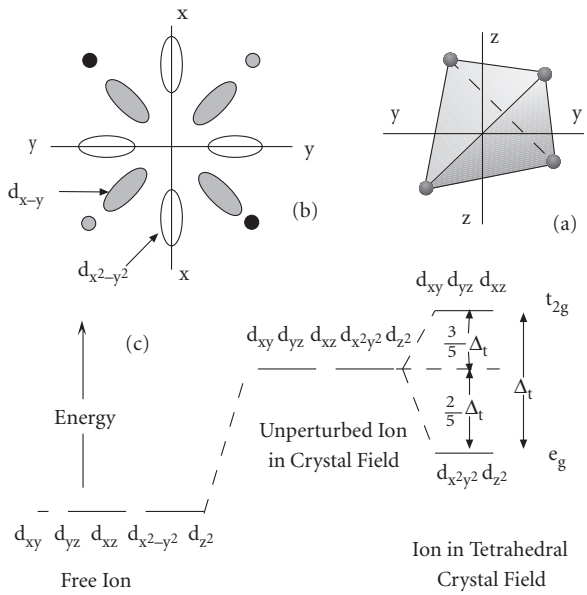

Figure 7.19 (a) Orientation of ligands and Cartesian coordinates for a metal ion in tetrahedral coordination. (b) Orientation of ligands (points) and d_{xy} (shaded) and $d_{x^2-y^2}$ (unshaded) orbitals in the $x - y$ plane of a metal in tetrahedral coordination. Black points are in front of plane of orbitals, gray points are behind the plane. (c) Energy-level diagram for *d* orbitals of a free transition metal ion, and an ion in a spherically symmetric crystal field and a tetrahedral crystal field. Adapted from Burns (1970).

In tetrahedral coordination (Figure 7.19), the e_g orbitals become more stable than the t_{2g} orbitals, but the tetrahedral crystal-field splitting parameter, Δ_t, is smaller than Δ_o. Other things being equal, $\Delta_t = 4/9\Delta_o$.

The crystal field splitting parameter, Δ, depends on a number of things, but some generalizations can be made:

1. Values of Δ are higher for +3 ions than +2 ions.
2. The values are 30% higher for each succeeding transition element (left to right in the periodic table).
3. Δ depends on the ligands coordinating the transition metal. Δ may be arranged to increase as follows: halides < OH^- (hydroxides) < silicates < H_2O < SO_4.
4. Δ depends on the symmetry of the coordinating ligands (as we have seen).

5. Δ varies with interatomic distance (inversely proportional to the 5th power).

In silicates, oxygen atoms frequently form distorted coordination polyhedra about cations, and metal–oxygen interatomic distances are not constant. Distortion of coordinated polyhedra is expected from the *Jahn-Teller theorem*, which states that if the ground state of a molecule is degenerate, it will distort to make one of the energy levels more stable (Figure 7.20). For example, if one of the *d* orbitals is filled or empty while another is half-filled, the environment about the transition metal ion is predicted to distort spontaneously to a different geometry in which a more stable electronic configuration is attained by making the occupied orbital lower in energy. Further splitting of *d* orbital energy levels occurs when transition metal ions are in distorted coordination.

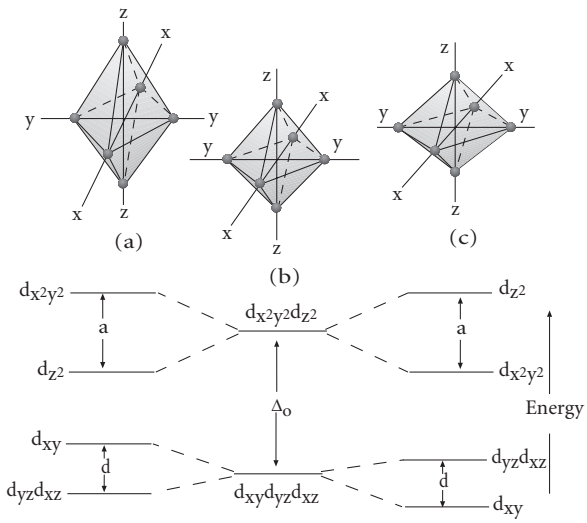

Figure 7.20 Arrangement of ligands and energy levels for (a) an octahedral site distorted along the *z*-axis; (b) an undistorted site; and (c) an octahedral site distorted along the *y*-axis. Burns (1970). Reprinted with the permission of Cambridge University Press.

This can be illustrated for the case of Mn^{3+} in octahedral coordination with oxygen. The Mn^{3+} ion has the high-spin configuration (Table 7.6) in which each t_{2g} orbital is occupied by one electron and the fourth electron may occupy either of the e_g orbitals. If the four oxygen atoms in the *x*–*y* plane move toward, and the two oxygens along the *z*-axis move away from, the central Mn^{3+} ion (Figure 7.20a), then the one e_g electron will favor the d_{z^2} orbital in which the repulsion by the O ions is smaller than in the $d_{x^2-y^2}$ orbital. Thus the e_g orbital group separates into two energy levels with the d_{z^2} becoming more stable. The t_{2g} orbital group is also split, with the d_{xz} and d_{yz} becoming more stable than the d_{xy} orbital. If the two O ions along the *z*-axis move closer to the Mn^{3+} ion (Figure 7.20c), the $d_{x^2-y^2}$

Table 7.6 Electronic configurations and crystal field stabilization energies of first transition series metal ions in octahedral configuration. From Burns (1970). Reprinted with the permission of Cambridge University Press.

Number of 3*d* electrons	Ion	High spin state				Low spin state			
		Electronic configuration		Unpaired electrons	CFSE	Electronic configuration		Unpaired electrons	CFSE
		t_{2g}	e_g			t_{2g}	e_g		
0	Sc^{3+}, Ti^{4+}			0	0			0	0
1	Ti^{3+}	↑		1	$2/5\Delta_o$	↑		1	$2/5\Delta_o$
2	Ti^{2+}, V^{3+}	↑↑		2	$4/5\Delta_o$	↑↑		2	$4/5\Delta_o$
3	V^{2+}, Cr^{3+}, Mn^{4+}	↑↑↑		3	$6/5\Delta_o$	↑↑↑		3	$6/5\Delta_o$
4	Cr^{2+}, Mn^{3+}	↑↑↑	↑	4	$3/5\Delta_o$	↑↓↑↑		2	$8/5\Delta_o$
5	Mn^{2+}, Fe^{3+}	↑↑↑	↑↑	5	0	↑↓↑↓↑		1	$10/5\Delta_o$
6	Fe^{2+}, Co^{3+}, Ni^{3+}	↑↓↑↑	↑↑	4	$2/5\Delta_o$	↑↓↑↓↑↓		0	$12/5\Delta_o$
7	Co^{2+}, Ni^{3+}	↑↓↑↓↑	↑↑	3	$4/5\Delta_o$	↑↓↑↓↑↓	↑	1	$9/5\Delta_o$
8	Ni^{2+}	↑↓↑↓↑↓	↑↑	2	$6/5\Delta_o$	↑↓↑↓↑↓	↑↑	2	$6/5\Delta_o$
9	Cu^{2+}	↑↓↑↓↑↓	↑↓↑	1	$3/5\Delta_o$	↑↓↑↓↑↓	↑↓↑	1	$3/5\Delta_o$
10	Zn^{2+}	↑↓↑↓↑↓	↑↓↑↓	0	0	↑↓↑↓↑↓	↑↓↑↓	0	0

becomes more stable than the d_{z^2}. In either of the distorted environments, the Mn^{3+} becomes more stable than in an undistorted octahedral site. Transition metals subject to Jahn-Teller distortions in octahedral coordination are those with d^4, d^9, and low-spin d^7 configurations, in which one or three electrons occupy e_g orbitals. Looking at Table 7.6, we can see that these are Cr^{2+}, Mn^{3+}, Cu^{2+}, Co^{2+} and Ni^{3+} ions.

As noted, electronic transition energies are related to color. Because of the distortion, additional electronic transitions become possible. The differing probabilities of the various electronic transitions in polarized radiation is one of the causes of *pleochroism*[*] in minerals.

Crystal-field effects lead to irregularities in the interatomic distances, or ionic radii of transition metals. As you might expect, they depend on the nature of the site, and for a given site, there need not be a smooth contraction of interatomic distances with increasing atomic number.

The application of crystal field theory is restricted to compounds where the transition metal forms a dominantly ionic bond with surrounding ligands. In sulfides, and related minerals, the effects of covalent bonding, in which the orbitals become hybridized, must be considered, but such consideration is beyond the scope of our treatment.

7.5.1 Crystal field influences on transition metal partitioning

We can now return to the transition metals and crystal-field theory to explain some of the peculiarities of their behavior. We noted that the energy of some *d* orbitals is reduced (stabilized) by the effects of the electrostatic field of coordinating ligands in both octahedral and tetrahedral sites, and that the octahedral CFSE is always greater than the tetrahedral CFSE. We now introduce one more quantity: the octahedral site preference energy (OSPE), which is defined as the octahedral CFSE minus the tetrahedral CFSE. Table 7.7 lists these energies for various first transition series metals. Silicate melts contain both octahedral and tetrahedral sites, but transition metals, with a few exceptions, occupy only octahedral sites in silicate minerals. Thus the OSPE is an indicator of the preference of the transition ion for solid phases over liquid phases: the higher the OSPE, the more readily it is

Table 7.7 Crystal-field splittings and stabilization energies in transition metal ions.

Number of 3*d* electrons	Ion	Electronic configuration		Δ (cm^{-1}) $M(H_2O)^{n+}_{6(aq)}$	CFSE Hydrate (kJ/mole)	Octahedral CFSE (kJ/mole)	Tetrahedral CFSE (kJ/mole)	Octahedralsite preference energy (kJ)
1	Ti^{3+}	$(t_{2g})^1$		20300	$2/5\Delta = 97.1$	87.4	58.6	28.9
2	V^{3+}	$(t_{2g})^2$		17700	$4/5\Delta = 169.0$	160.2	106.7	53.6
3	Cr^{3+}	$(t_{2g})^3$		17400	$6/5\Delta = 249.4$	224.7	66.9	157.7
4	Cr^{2+}	$(t_{2g})^3$	$(e_g)^1$	13900	$3/5\Delta = 99.6$	100.7	29.3	71.1
4	Mn^{3+}	$(t_{2g})^3$	$(e_g)^1$	21000	$3/5\Delta = 150.6$	135.6	40.2	95.4
5	Mn^{2+}	$(t_{2g})^3$	$(e_g)^2$	7800	0	0	0	0
5	Fe^{3+}	$(t_{2g})^3$	$(e_g)^2$	13700	0	0	0	0
6	Fe^{2+}	$(t_{2g})^4$	$(e_g)^2$	10400	$2/5\Delta = 49.8$	49.8	33.1	16.7
6	Co^{3+}	$(t_{2g})^6$		18600	$12/5\Delta = 533.5$*	188.3	108.8	79.5
7	Co^{2+}	$(t_{2g})^5$	$(e_g)^2$	9300	$4/5\Delta = 89.1$	92.9	61.9	31.0
7	Ni^{3+}	$(t_{2g})^6$	$(e_g)^1$	–	$9/5\Delta =$			
8	Ni^{2+}	$(t_{2g})^6$	$(e_g)^2$	8500	$6/5\Delta = 29.6$	122.2	36.0	86.2
9	Cu^{2+}	$(t_{2g})^6$	$(e_g)^3$	12600	$3/5\Delta = 21.6$	90.4	26.8	63.6

* Low-spin complexes. The calculated CFSE must be reduced by the energy required to couple two electrons in a *t2g* orbital. Data from Orgel (1966) and McClure (1957).

* Pleochroism refers to the property possessed by some crystals of exhibiting different colors when viewed along different axes in polarized light.

partitioned into a solid phase. Predicted order of uptake is: Ni > Co > Fe^{2+} > Mn for +2 ions and Cr > V > Fe^{3+} for +3 ions, which agrees with observation. Since the number of octahedral sites in the liquid decrease with increasing SiO_2 concentration, crystal-field theory explains why Ni partition coefficients are highly composition-dependent, increasing with increasing SiO_2 concentration.

It should be emphasized that there are no crystal field effects for transition metals such as Sc^{2+}, Ti^{4+}, Y^{3+}, Zr^{4+}, Nb^{5+}, Hf^{4+}, and Ta^{5+}, where the *d* electrons are not present in the ion, or where the *d* shell is completely filled (Zn^{2+}) in the usual valence state, at least when the electrons are in their ground state. However, color, which arises from excitation of electrons into higher orbitals and subsequent decay to the ground state, may still relate to crystal field effects even when the *d* orbitals are not filled in the ground state. The second and third transition series metals for which crystal-field effects are expected are all highly siderophile or chalcophile and highly depleted in the Earth's crust and mantle. Little information is available on their behavior in silicate systems.

An understanding of crystal-field theory solves an interesting dilemma. A phase (T–X) diagram for the binary system Mg_2SiO_4–Ni_2SiO_4 is shown schematically in Figure 7.21. It is apparent from a quick glance that for any coexisting liquid and solid in the system, the solid will be poorer in Ni than the liquid, i.e., $(Ni/Mg)_{ol} < (Ni/Mg)_{liq}$. However, olivine crystallizing from basaltic liquids is always richer in Ni than the liquid. The reason for this is that in the pure olivine system, only octahedral sites exist in the melt and the solid, and thus Ni has no particular preference for the solid due to crystal-field effects. But basaltic melts have both tetrahedral and octahedral sites, while olivine has only octahedral sites (available to Ni). The greater availability of octahedral sites in the solid provides an added incentive for Ni to partition into olivine relative to basaltic liquid.

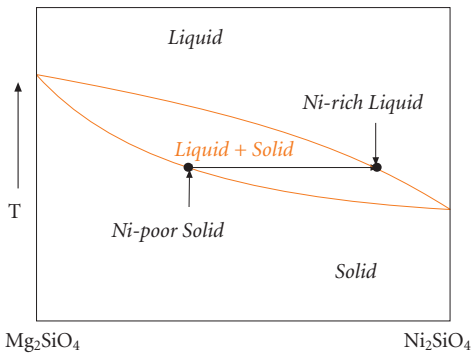

Figure 7.21 Schematic phase diagram for the system forsterite–Ni olivine showing Ni-poor olivine in equilibrium with Ni-rich liquid.

7.6 TRACE ELEMENT DISTRIBUTION DURING PARTIAL MELTING

In igneous geochemistry, trace elements are useful in understanding magmatic processes and in evaluating the composition of magma sources such as the mantle and lower crust. To make use of trace elements in such studies, we need to understand how magmatic processes such as partial melting and fractional crystallization will affect trace element abundances.

The task of the igneous geochemist is often to make inferences about the sources of magma, the mantle and lower crust, from the composition of the magmas themselves. This can be done through a mathematical model of melting. In the following sections, we will consider two simple alternative models of melting: batch, or equilibrium, melting, and fractional melting. In fractional melting, the melt is extracted as soon as it is created, and only an infinitesimal increment of melt will be in equilibrium with the solid residue at any given time. In batch melting, a finite amount of melt, for example 5 or 10%, is produced and equilibrates completely with the solid residue.

Once a melt is created and begins to rise, it may further interact with the surrounding "wallrock". We will also consider one possible model of this interaction: "zone refining". Choosing between alternative models of partial melting requires a knowledge of how melting and melt extraction actually occurs. Unfortunately, melting and melt extraction in the Earth remain poorly understood because we are unable to observed them directly. Although melting experiments are useful in determining phase relationships, melting temperatures, and distribution coefficients, they do not provide much direct information on

how melt is extracted. By and large, our knowledge of the melt extraction process comes from indirect inferences. Rarely, we can identify partial melting residues that have been tectonically emplaced at the surface of the Earth, and studies of these have provided some insights into the melting process. We will consider some of these insights in a subsequent section.

7.6.1 Equilibrium or batch melting

Equilibrium crystallization or melting implies complete equilibration between solid and melt. This means that the entire batch equilibrates with the residue before it is removed. From mass balance we may write:

$$C_i^o = C_i^s(1-F) + C_i^\ell F \qquad (7.41)$$

where i is the element of interest, C° is the original concentration in the solid phase (and the concentration in the whole system), C^ℓ is the concentration in the liquid, C^s is the concentration remaining in the solid and F is the melt fraction (i.e., mass of melt/mass of system). Since D = C^s/C^ℓ, and rearranging:

$$C_i^o = C_i^\ell D_i^{s/\ell}(1-F) + C_i^\ell F$$

or:

$$\boxed{\frac{C_i^\ell}{C_i^o} = \frac{1}{D^{s/\ell}(1-F)+F}} \qquad (7.42)$$

This equation is an extremely useful one and describes the relative enrichment or depletion of a trace element in the liquid as a function of degree of melting. Two approximations are often useful and give us a feel for this equation. First consider the case where $D << F$. In this case $C^\ell/C^\circ \approx 1/F$, that is, the enrichment is inversely proportional to the degree of melting. This is the case for highly incompatible elements at all but the smallest degrees of melting. Now consider the case where F approaches 0. In this case $C^\ell/C^\circ \approx 1/D$, the enrichment is inversely proportional to the partition coefficient. Thus the maximum enrichment possible in a partial melt is $1/D$. For highly compatible elements, that is, those with large D such as Ni, the depletion in the melt is $1/D$ when F is small and is relatively insensitive to F.

7.6.2 Fractional melting

Now consider the case where only an infinitesimally small amount of melt equilibrates with the solid residue, in other words, imagine we remove the liquid as fast as we make it. If i^s is the mass of element i in the solid phase being melted, S the mass of the solid phase, L the mass of the liquid phase, i^l the mass of i in the liquid, $S°$ the original mass of the solid (and mass of the system), and $i°$ the original mass of i in the solid (and system), then:

$$C_i^s = \frac{i^s}{S} = \frac{i° - i^l}{S° - L} \quad \text{and} \quad C_i^\ell = \frac{1}{D_i}\frac{i° - i^\ell}{S° - L} = \frac{di^\ell}{dL}$$

This can be rearranged so that we can integrate it to obtain:

$$\boxed{\frac{C_i^\ell}{C_i^o} = \frac{1}{D}(1-F)^{1/D-1}} \qquad (7.43)$$

If we subsequently mix the various melt fractions produced over a melt interval from 0 to F, the composition of this *aggregate liquid*, $\bar{C}$ is:

$$\boxed{\frac{\bar{C}_i^\ell}{C_i^o} = \frac{1}{F}\left(1-(1-F)^{1/D_i}\right)} \qquad (7.44)$$

Figure 7.22 illustrates the variation of the liquid enrichment (C^ℓ/C^o) with degree of melting for both batch and fractional melting.

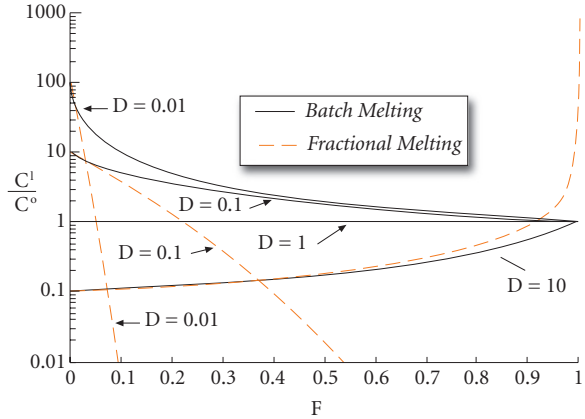

Figure 7.22 Variation in C^ℓ/C^o with degree of melting, F, for various partition coefficients for batch and fractional melting.

The aggregate liquid of fractional melting, which may be the most realistic of the three equations we have considered so far, follows a trend close to that of batch melting.

7.6.3 Zone refining

If melt percolates slowly through the source region, trace element fractionation may be best approximated by equations governing zone refining. The term zone refining comes from the industrial purification process in which a melt zone is caused to migrate along a column of material. Several passes of this process efficiently extract low melting-temperature components. The relevant equation is:

$$\frac{C_i^\ell}{C_i^o} = \frac{1}{D_i} - \left(\frac{1}{D_i} - 1\right) e^{-D_i R} \qquad (7.45)$$

where R is the ratio of host, or wallrock, to melt. Note that for large R, $C^\ell/C^o \sim 1/D$.

7.6.4 Multiphase solids

The above equations are relevant when the solid undergoing melting is homogenous. If it consists of several phases, we need to replace D with a *bulk* distribution coefficient, which is simply the weighted mean of the individual solid/liquid partition coefficients:

$$\bar{D}_i = D_i^o = \sum_\phi m_\phi D_i^{\phi/\ell} \qquad (7.46)$$

where m is simply the *modal mass fraction* of phase ϕ, that is, the fraction of phase ϕ as it exists in the rock.

In general, minerals do not enter the melt in the proportion in which they exist in a rock (i.e., their modal proportions). Thus a realistic melting model requires that we modify our equations to account for this. We need to define a new parameter P, which is simply the average individual partition coefficients weighted according to the proportions in which the minerals enter the melt:

$$P_i = \sum_\phi p_\phi D_i^{\phi/\ell} \qquad (7.47)$$

where p is the proportion in which phase ϕ enters the melt. It is often assumed that the p^ϕ values are constants. In reality, they will be functions of F. The equations for batch and fractional melting in this *non-modal melting* case become:

Non-modal batch melting:

$$\frac{C_i^\ell}{C_i^o} = \frac{1}{F(1-P_i) + D_i^o} \qquad (7.48)$$

Non-modal fractional melting

$$\frac{C_i^\ell}{C_i^o} = \frac{1}{D_i^o}\left(1 - \frac{P_i F}{D_i^o}\right)^{1/P_i - 1} \qquad (7.49)$$

The aggregate liquid for non-modal fractional melting is given by:

Aggregate:

$$\frac{\bar{C}_i^\ell}{C_i^o} = \frac{1}{F}\left(1 - \left(1 - \frac{P_i F}{D_i^o}\right)^{1/P_i}\right) \qquad (7.50)$$

These equations are from Shaw (1970); their use is illustrated in Example 7.3.

7.6.5 Continuous melting

In most circumstances, the way in which rock melts in the Earth is probably intermediate between our batch and fractional melting models: only part of the melt is extracted continuously, while some fraction remains to fill the pore spaces between the mineral grains. This process has been called *continuous melting*. Let's look at how we can modify our fractional melting equation (eqn. 7.43) for this situation.

Consider a rock undergoing melting. We assume that it has a melt-filled porosity of ϕ, where ϕ is defined by mass. We can replace the partition coefficient in eqn. 7.43 with an effective partition coefficient, D', which takes account of a fraction of liquid, ϕ, in the rock with a partition coefficient of 1 (Albarède, 1995). Equation 7.43 thus becomes:

$$\frac{C_i^\ell}{C_i^o} = \frac{1}{D_i'}(1-F)^{1/D_i' - 1} \qquad (7.51)$$

F in this case is the fraction of melt extracted, which differs from the total amount of melt produced by an amount equal to ϕ. D' is

Example 7.3 Modelling partial melting

Geochemists are often interested in the ratios of incompatible trace elements. For one thing, ratios of incompatible elements are less affected by fractional crystallization than are trace element abundances. To illustrate the effect of partial melting on a trace element ratio, we will calculate how the ratio of La to Sm varies in basalts produced by different extents of melting in the mantle.

We need to make some assumptions about the composition and mineralogy of the mantle. These assumptions are: (1) the mantle "source" is composed of 58% olivine, 27% orthopyroxene, 12% clinopyroxene, and 3% spinel; (2) these minerals enter the melt in the proportions 20% olivine, 25% orthopyroxene, 45% clinopyroxene, and 10% spinel; (3) that this source contains 1 ppm La and 1 ppm Sm. Using the partition coefficients for peridotite mantle listed below, we calculate the La and Sm concentrations at 2% and 10% melting using the batch melting model.

Partition coefficients

	Ol	Opx	Cpx	Spinel
La	0.0003	0.002	0.053	0.01
Sm	0.0013	0.011	0.36	0.01

Our first step is to calculate the D_o and P values for each element using eqns. 7.46 and 7.47. Doing so, we find $D_{La} = 0.007$, $D_{Sm} = 0.047$, $P_{La} = 0.025$, $P_{Sm} = 0.166$. Using eqn. 7.48, we find that at 10% melting, [La] = 9.5 ppm and [Sm] = 7.66 ppm. So a 10% melt (F = 0.1) of a mantle having La/Sm = 1 will have La/Sm = 9.5/7.66 = 1.25. For the same calculation at 2% melting we obtain [La] = 37.3 ppm and [Sm] = 15.65 ppm and La/Sm = 2.38. Thus at a fairly large degree of melting (10%), the La/Sm ratio was only 25% greater than that of the source. At a small degree of melting, the La/Sm ratio was more than a factor of 2 greater than that of the source.

related to the usual partition coefficient, D, (eqn. 7.1) as:

$$D_i' = (1-\phi)D_i + \phi \qquad (7.52)$$

The exponential term in eqn. 7.51, $1/D' - 1$, is related to D by:

$$\frac{1}{D_i'} - 1 = \frac{1-\phi}{(1-\phi)D_i + \phi}(1-D) \qquad (7.53)$$

Substituting these back into eqn. 7.51, our expression for continuous melting written in terms of the usual partition coefficient is:

$$\frac{C_i^\ell}{C_i^o} = \frac{1}{(1-\phi)D_i + \phi}(1-F)^{\frac{(1-\phi)(1-D_i)}{(1-\phi)D_i+\phi}} \qquad (7.54)$$

Porosity is normally defined in terms of volume, but the above equations use a porosity defined in terms of mass. The relationship between the mass porosity and the volume porosity is:

$$\phi = \frac{\rho_\ell \varphi}{\rho_s(1-\varphi) + \rho_\ell \varphi} \qquad (7.55)$$

where ϕ is the mass porosity, φ volume porosity, ρ_s is the density of the solid and ρ_ℓ is the density of the liquid.

We can also derive an equation for an aggregate continuous melt simply by replacing D with D' in eqn. 7.44. Figure 7.23 compares continuous and fractional melting for $D = 0.0001$ and $\phi = 0.001$. Leaving residual melt in the pores has the effect of buffering the depletion of the solid, so that the concentration of an incompatible element does not decrease as fast in the case of continuous melting as for fractional melting. As Figure 7.23 shows, for high values of F, the aggregate melts produced by fractional and continuous melting have almost identical compositions. The compositions of the residual solids, however, will be far different, with the residue of fractional melting being far

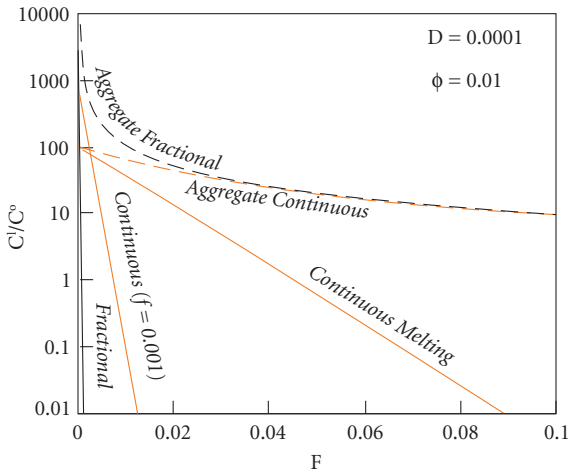

Figure 7.23 Comparison of continuous and fractional melting for D = 0.0001 and $\phi = 0.01$. The aggregate melt is similar in both cases when F is greater than about 2%. A separate curve for continuous melting is shown for $\phi = 0.001$.

more depleted in incompatible elements than the residue of batch melting.

7.6.6 Constraints on melting models

To summarize the discussion above, we may say that the concentration of a trace element in a melt is a function of: (1) the solid phases (i.e., minerals) present in the system before and during melting; (2) the extent of melting (i.e., *F*); (3) the manner of melting (e.g., fractional vs. batch); (4) the concentration of the element in the original solid (i.e., *C*°); and (5) the partition coefficients. The partition coefficients, as we have seen, are functions of temperature, pressure, and composition of the phases involved. Two tasks of trace element geochemistry are to deduce something about the melting process and about the composition of the source of magmas. If we are to use trace elements for these purposes, it is essential we independently constrain some of these variables.

Most magmas are generated by partial melting of the upper mantle. Although temperature increases with depth in the mantle, the solidus temperature (i.e., the temperature where melting begins) increases more rapidly, so that the deep mantle is generally well below its solidus.* Though they have played a very important role in the evolution of the Earth, magmas produced by melting of the deep mantle are very much rarer. So our discussion here will be limited to the melting process in the upper mantle. The phases present in the upper mantle, and their compositions, are discussed in more detail in Chapter 11, so we will omit that topic from the discussion here.

7.6.6.1 Relationship between melt fraction and temperature and pressure

We can shorten our list of variables if we can somehow relate the degree of melting to temperature and ultimately to pressure. We can do this through a simplified thermodynamic analysis.

Most melting in the mantle, with the notable and important exception of subduction zones, appears to result from decompression: packets of mantle moving upward. Pressure in the Earth is related to depth, (*h*), by the simple relationship:

$$\frac{dP}{dh} = \rho g \qquad (7.56)$$

where ρ is density and *g* is the acceleration of gravity. For a typical upper mantle density, pressure increases by about 1 GPa for every 35 km depth.

Because of the scales generally involved (kilometers to hundreds of kilometers) and the low thermal conductivity of rock, it is reasonable to assume that a rising packet of mantle is adiabatic. As we learned in Chapter 2, this means it can do work or have work done on it, but it does not exchange heat with its surroundings (i.e., $dQ = 0$). We also learned in Chapter 2 that an adiabatic system is an isoentropic one (i.e., $dS = 0$). The constraint that the system is isoentropic allows us to relate the amount of melting that will occur to the temperature and pressure of the rising mantle.

* Recent seismic studies suggest the possible presence of melt pockets in the lowermost mantle, near the core–mantle boundary.

The variation of entropy with temperature and pressure can be expressed as:

$$dS = \left(\frac{\partial S}{\partial T}\right)_P dT + \left(\frac{\partial S}{\partial P}\right)_T dP \qquad (7.57)$$

Substituting eqns. 2.105 and 2.106 into eqn. 7.57, we have:

$$dS = \frac{C_P}{T} dT - \alpha V dP \qquad (7.58)$$

Since the system is isoentropic, $dS = 0$, and we can solve eqn. 7.58 to obtain:

$$\left(\frac{\partial T}{\partial P}\right)_S = \frac{T\alpha V}{C_P} \qquad (7.59)$$

This equation describes the *adiabat*, the P–T path that adiabatically rising mantle follows. (By the way, we can see that the adiabat will be curved, since its slope depends on T). The solidus temperature will also change with pressure, and its slope is given by the *Clapeyron equation* (eqn. 3.3):

$$\left(\frac{dT}{dP}\right)_{sol} = \frac{\Delta V_m}{\Delta S_m}$$

The slope of the solidus is steeper than that of the adiabat, so that rising mantle will eventually intersect the solidus (Figure 7.24). For simplicity, let's assume the solid consists of a single phase. When the solidus is reached, the system will consist of two phases, solid and liquid, and we can write one version of eqn. 7.57 for the solid and one version for any melt that has formed. Now let's specify that the two phases coexist at equilibrium along a univariant reaction curve, whose slope in T–P space is $(dT/dP)_{2\phi}$. We can solve eqn. 7.57 to determine how entropy of each phase changes with pressure, for example, for the solid:

$$\frac{dS^s}{dP} = \frac{C_P^s}{T}\left(\frac{dT}{dP}\right)_{2\phi} - \alpha^s V^s \qquad (7.60)$$

The total specific entropy (i.e., entropy per unit mass) of the system, S_o, can be expressed as the sum of the entropy of the solid and the melt.

$$FS^\ell + (1-F)S^s = S_0 \qquad (7.61)$$

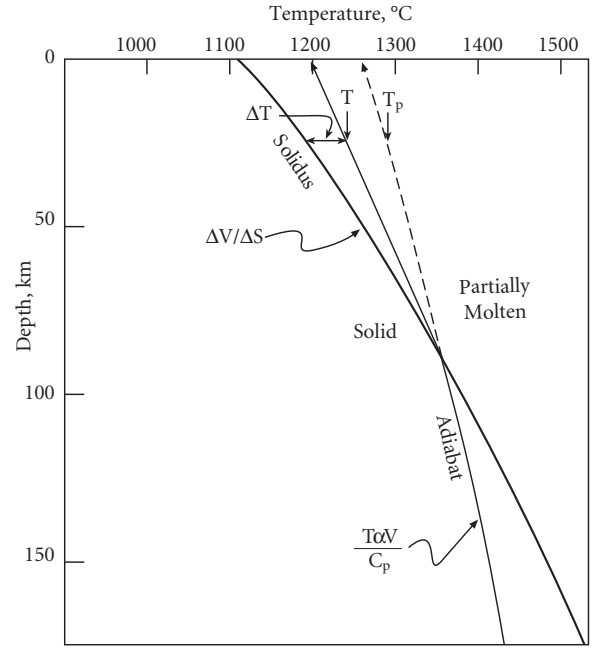

Figure 7.24 Representation of melting of an ascending packet of mantle in temperature and pressure space. Below the solidus, the mantle rises along the adiabat. Once the packet intersects the solidus, the T–P path of the mantle packet is deflected, as shown by the solid line marked T.

where S^ℓ and S^s are specific entropies of the melt and solid respectively and F is the fraction of melt. If we solve eqn. 7.61 for F, we have:

$$F = \frac{S_0 - S^s}{S^\ell - S^s} \qquad (7.62)$$

The term $S^\ell - S^s$ is just entropy of melting, ΔS_m, so eqn. 7.62 can be written as:

$$F = \frac{S_0 - S^s}{\Delta S_m} \qquad (7.63)$$

As long as the melt is not extracted, the system remains isoentropic and S_0 is a constant; however, neither S^ℓ nor S^s are necessarily constant. Let's assume for the moment that ΔS_m is also constant (equivalent to assuming that S^ℓ and S^s change in an identical way). If we now differentiate eqn. 7.63 with respect to pressure, we have:

$$\left(\frac{\partial F}{\partial P}\right)_S = \frac{1}{\Delta S_m}\left(\frac{C_P^s}{T}\left(\frac{dT}{dP}\right)_{2\phi} - \alpha^s V^s\right) \quad (7.64)$$

Equation 7.64 shows that even assuming that all the thermodynamic parameters therein are constant, the amount of melt produced by rising mantle will be a function of its temperature.

Once melting begins, the rising mantle follows a P–T path that is steeper than adiabatic (Figure 7.24), since some energy is consumed in melting. Let's call the temperature that the system would have attained, had melting not occurred, the potential temperature, T_p. The difference between that temperature and the actual temperature T is related to the entropy change during melting, ΔS_m. We can determine the entropy change due to the difference between T and T_p by integrating eqn. 2.105:

$$\Delta S = \int_T^{T_p} \frac{C_P}{T} dT \quad (7.65)$$

Since we are interested in a simple, approximate analysis, let's assume that C_P is constant. In that case, eqn. 7.65 becomes:

$$\Delta S = C_p \ln \frac{T_p}{T} \quad (7.66)$$

To find a simple linear solution, let's approximate eqn. 7.66 with a Taylor series expansion about T_{act}, which yields:

$$\Delta S \cong \frac{C_p}{T}(T_p - T) \quad (7.67)$$

As long as melt has not been lost, the system remains isoentropic, so the entropy difference in eqn. 7.67 must simply be the entropy consumed in melting:

$$\Delta S = \Delta S_m F \quad (7.68)$$

Equating the two, we have:

$$\Delta S_m F \cong \frac{C_p}{T}(T_p - T) \quad (7.69)$$

Rearranging, and letting $\Delta T = (T_{pot} - T)$, we have:

$$T_{pot} - T \cong \frac{T}{C_p}\Delta S_m F \quad (7.70)$$

This difference, $T_{pot} - T$ is the temperature deflection due to melting in the P–T path and is shown in Figure 7.24. If we differentiate eqn. 7.70 with respect to P (and still holding S constant), we have:

$$\left(\frac{\partial (T_p - T)}{\partial P}\right)_S \cong \frac{\Delta S_m}{C_p}\left(\frac{\partial (TF)}{\partial P}\right)_S = \frac{\Delta S_m}{C_p}\left[F\left(\frac{\partial T}{\partial P}\right)_S + T\left(\frac{\partial F}{\partial P}\right)_S\right]$$

and finally:

$$\left(\frac{\partial \Delta T}{\partial P}\right)_S \cong \frac{\Delta S_m}{C_p} F\left(\frac{\partial T}{\partial P}\right)_S + \frac{\Delta S_m}{C_p} T\left(\frac{\partial F}{\partial P}\right)_S \quad (7.71)$$

Solving for $(\partial T/\partial P)_S$, we have:

$$\left(\frac{\partial T}{\partial P}\right)_S \cong \left(\frac{\partial T_p}{\partial P}\right)_S - \frac{T}{C_p}\Delta S_m\left(\frac{\partial F}{\partial P}\right)_S \quad (7.72)$$

The term $(\partial T_{pot}/\partial P)_S$ is just the adiabatic gradient, given by eqn. 7.58, and substituting that into eqn. 7.72 we have:

$$\left(\frac{\partial T}{\partial P}\right)_S \cong \frac{T\alpha V}{C_P} - \frac{T}{C_p}\Delta S_m\left(\frac{\partial F}{\partial P}\right)_S \quad (7.73)$$

Equation 7.73 describes the P–T path that a system undergoing isoentropic melting will follow as it rises.

The degree of melting will be a function of excess temperature, that is, the difference between the solidus temperature and the actual temperature, which we shall call ΔT. In Figure 7.24, ΔT can be found by subtracting the solidus temperature from the temperature path of the mantle packet:

$$\left(\frac{\partial \Delta T}{\partial P}\right)_S \cong \left[\frac{T\alpha V}{C_P} - \frac{T}{C_p}\Delta S_m\left(\frac{\partial F}{\partial P}\right)_S\right] - \left(\frac{\partial T}{\partial P}\right)_{solidus} \quad (7.74)$$

There have been many attempts to determine the relationship between melting and temperature for mantle materials. Such melting curves are notoriously difficult to determine. Figure 7.25 shows an experimentally determined melting curve for a peridotite

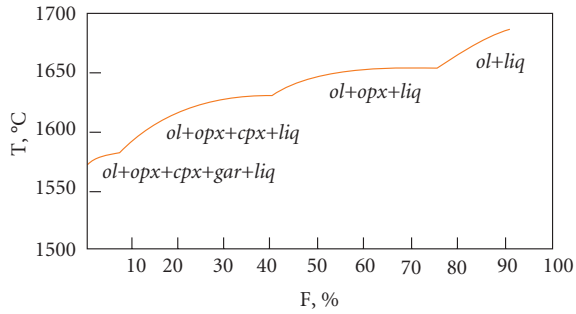

Figure 7.25 Relationship between extent of melting, F, and temperature in peridotite at 3.5 GPa determined experimentally in graphite capsules by Harrison (1979). Kinks in the curve correspond to consumption of phases, in the order garnet (gar), clinopyroxene (cpx), and orthopyroxene (opx).

composition at 3.5 GPa. The curve has several breaks in slope that correspond to elimination of phases. Despite the kinks, one can extract from this kind of experiment a relationship between degree of melting and excess temperature, that is, a value for $(\partial F/\partial T)_P$. For example, Langmuir *et al.* (1993) adopted a value of about 0.00285 for $(\partial F/\partial T)_P$ below 22% melting, and 0.0015 for $(\partial F/\partial T)_P$ above 22% melting. We want to incorporate this information into our analysis. We do this as follows. First, we express the variation in temperature as a function of melt fraction and pressure:

$$dT = \left(\frac{\partial T}{\partial P}\right)_F dP + \left(\frac{\partial T}{\partial F}\right)_P dF \qquad (7.75)$$

If we differentiate eqn. 7.75 with respect to pressure, specifying that entropy be held constant, we can derive the following relationship:

$$\left(\frac{\partial T}{\partial P}\right)_S = \left(\frac{\partial T}{\partial P}\right)_F + \left(\frac{\partial T}{\partial F}\right)_P \left(\frac{\partial F}{\partial P}\right)_S$$

This can be substituted into eqn. 7.72 to obtain:

$$\left(\frac{\partial T}{\partial P}\right)_F + \left(\frac{\partial T}{\partial F}\right)_P \left(\frac{\partial F}{\partial P}\right)_S \cong \frac{T\alpha V}{C_P} - \frac{T}{C_p}\Delta S_m \left(\frac{\partial F}{\partial P}\right)_S \qquad (7.76)$$

Rearranging:

$$\left(\frac{\partial T}{\partial P}\right)_F - \frac{T\alpha V}{C_P} \cong \left[-\frac{T}{C_p}\Delta S_m - \left(\frac{\partial T}{\partial F}\right)_P\right]\left(\frac{\partial F}{\partial P}\right)_S$$

and finally:

$$\left(\frac{\partial F}{\partial P}\right)_S \cong \frac{\dfrac{T\alpha V}{C_P} - \left(\dfrac{\partial T}{\partial P}\right)_F}{\dfrac{T}{C_p}\Delta S_m + \left(\dfrac{\partial T}{\partial F}\right)_P} \qquad (7.77)$$

Equation 7.77 gives the *melt fraction as a function of pressure above the pressure where the mantle intersects the solidus*.

Let's now attempt to evaluate eqn. 7.77 by substituting some real values into it. The term $(\partial T/\partial P)_F$ is the slope in T–P space of lines of constant melt fraction. We can make two simplifying assumptions: (1) the lines of constant melt fraction are parallel to the solidus; and (2) the solidus can be adequately described by a Clapeyron slope, eqn. 3.3 (because the composition of both melt and solid can vary in the real mantle, the solidus will not be a simple univariant curve described by the Clapeyron equation), so eqn. 7.77 becomes:

$$\left(\frac{\partial F}{\partial P}\right)_S \approx \frac{\dfrac{T\alpha V}{C_P} - \dfrac{\Delta V_m}{\Delta S_m}}{\dfrac{T}{C_p}\Delta S_m + \left(\dfrac{\partial T}{\partial F}\right)_P} \qquad (7.78)$$

The coefficient of thermal expansion, α, is about $3 \times 10^{-5}\,K^{-1}$, V is about 0.3175 cm^3/g (= 0.3175 JMPa^{-1}g^{-1}), and C_p is about 1.15 JK^{-1}g^{-1}. Thus the adiabatic gradient at 1673 K (1400°C) is about 12 K/GPa. The term $(\partial T/\partial F)_P$ is, of course, just the inverse of $(\partial F/\partial T)_P$ and has a value of 1/0.00285 = 350.88 K. ΔV_m is about 0.0434 cm^3/g (0.0434 JMPa^{-1}g^{-1}) and ΔS_m is about 0.362 JK^{-1}g^{-1}, which corresponds to a slope of the solidus of about 120 K/GPa. From this we calculate a value for $(\partial F/\partial P)_S$ of about –0.12 GPa^{-1}, or about –1.2%/kbar (it is negative because the extent of melt *increases* as pressure *decreases*). Of course, we have greatly simplified matters here by neglecting the pressure and temperature dependencies of all thermodynamic functions. Thus this relationship is only approximate, and considering the uncertainty in our assumptions and the thermodynamic parameters, this value could

lie anywhere between –0.08/GPa and –0.2/GPa. So, for example, if a rising packet of mantle intersects the solidus at 100 km depth (≈3 GPa), upon reaching a depth of 30 km (~1 GPa) that packet would have undergone 24% melting.

The solidus temperature of silicates can be substantially lowered by the addition of water and, at high pressures, of CO_2. In the presence of either H_2O or CO_2, the melting curve will be different from that shown in Figure 7.24, and the relationship we deduced between melt, temperature, and pressure will also be different.

A final point to make is that once melt is extracted, the system is no longer isoentropic because the extracted melt carries away some of the entropy of the system. Thus our analysis would be strictly limited to batch melting, where the melt remains in equilibrium with the solid. A complete treatment of the thermodynamics of melting, including fractional melting, can be found in Azimov *et al*. (1997). Morgan (2001) discusses the situation where the material undergoing melting is lithologically heterogeneous.

7.6.6.2 Mantle permeability and melt distribution and withdrawal

Whether the melting process approximates the batch (equilibrium) model or the fractional model depends upon the permeability of the source region. If the source region is highly permeable, melt will flow out as it is created, approximating the fractional melting model; if it is impermeable, it will build up in place before ascending, approximating the equilibrium model. Permeability depends upon the degree to which the melt is interconnected, and this in turn depends on the crystal–liquid interfacial energy.

We explored the effects of interfacial energy on nucleation in Chapter 5 (section 5.5.3.3). We found that the difference in interfacial energy determined the geometry of nucleation. Here we wish to consider the case of how a liquid will distribute itself between grains of a solid undergoing melting. We assume that the solid consists of a single phase (e.g., olivine) and that the interfacial energy between these grains is σ_{ss}. Now consider the intersection between three such grains (Figure 7.26). When melt is present, there

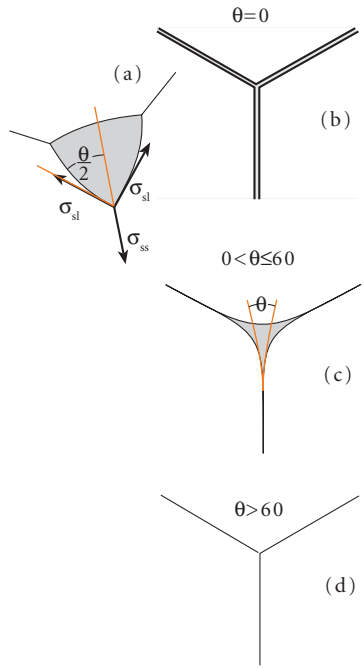

Figure 7.26 Relationship between dihedral angle, θ, and melt distribution at grain triple junctions. (a) The balance of solid–solid and solid–liquid interfacial energies, σ_{ss} and σ_{sl}, at the junction. (b) θ = 0, and the melt (shaded) is distributed along grain–grain boundaries as well as triple junctions. (c) The melt forms an interconnected network along grain triple junctions. (d) θ is greater than 60° and melt is present only at 4-grain junctions. After Kingery (1960) and Kohlstedt (1993).

will also be an interfacial energy between the grains and the melt, σ_{sm}. If θ is the angle formed by a melt pocket at a grain triple junction, the balance of forces may be described as:

$$\sigma_{ss} = 2\sigma_{s\ell} \cos\frac{\theta}{2} \qquad (7.79)$$

Rearranging, we have:

$$\cos\frac{\theta}{2} = \frac{\sigma_{ss}}{2\sigma_{s\ell}} \qquad (7.80)$$

and

$$\theta = 2\arccos\left(\frac{\sigma_{ss}}{2\sigma_{s\ell}}\right) \qquad (7.80a)$$

The bottom line is that the lower the solid–liquid interfacial energy, the more extensively melt will interconnect (the more extensively grains will "wet") and the more readily melt will flow. Considering eqn. 7.80 in greater detail reveals that, depending on the value of θ, the melt can distribute itself in number of ways. These are illustrated in Figure 7.26. The first case occurs when the solid–solid interfacial energy is twice that of the solid–melt interfacial energy; if so, then cos $\theta/2 = 1$ and $\theta \approx 0$. In this case, solid–solid interfaces are energetically unfavorable and melt will form a thin film that coats all grain boundaries (Figure 7.26b). The second case is where the solid–solid interfacial energy is more than 1.73 times but less than twice that of the solid–melt interfacial energy ($2\sigma_{sl} > \sigma_{ss} > 1.73\sigma_{sm}$), which corresponds to $0 < \theta < 60°$ (Figure 7.25c). In this case, the melt will form interconnected channels along grain triple junctions, as is illustrated in Figure 7.26, but is absent from grain–grain surfaces. The third case corresponds to $\sigma_{ss} < 1.73\sigma_{sl}$ and $\theta > 60°$ (Figure 7.25d). In this case, melt forms isolated pockets at junctions between 4 or more grains but is absent elsewhere. These pockets become connected only at relatively high melt fractions (several percent). Permeability will be high for the first two cases where melt forms films or channels that allow melt to flow, but low for the last case of isolated melt pockets. The interfacial energy, and hence θ, depends upon temperature, pressure, and the composition of the melt and solid phase, and hence will vary even within a single rock.

Scanning electron microscopy of experiments in which basaltic melt is allowed to come to textural equilibrium with olivine indicate that θ is characteristically between 25° and 50°. The dihedral angle is larger, typically greater than 60°, for junctions between pyroxene grains and for H_2O and CO_2 fluids (though addition of water to a silicate rock reduces θ). Since the upper mantle consists of over 60% olivine, however, it is likely that melt forms an interconnected network such as that illustrated in Figure 7.27, resulting in high permeability. Experiments in which melt is induced to migrate, either as a result of a gradient in melt fraction in the experimental charge or as a result of stress, confirm that permeability of mantle material undergoing melting will be high. From our perspective, this means melt is likely to be extracted fairly quickly after it is created, and that very small melt fractions, perhaps as low as 0.1%, can segregate from the mantle. Thus the fractional melting model may more closely approximate melting in the mantle.

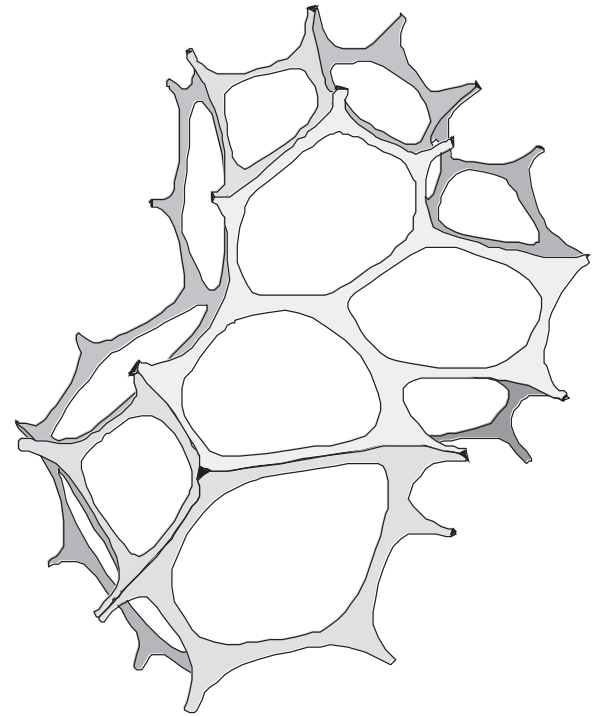

Figure 7.27 Three-dimensional network formed by melt along triple junctions of olivine grains. From Riley and Kohlstedt (1990). With permission from Elsevier.

Laporte (1994) carried out similar experiments with quartz and hydrous silicate melts and found that the dihedral is in the range of 12–18°, indicating a high ratio of σ_{ss}/σ_{sl}. This in turn indicates that the permeability within regions of the crust undergoing melting will be relatively high. However, the rate at which melt segregates from its source depends upon melt viscosity as well as permeability. Because the viscosity of even hydrous granitic magmas is four orders of magnitude greater than that of basalt, segregation of granitic melt requires a higher melt fraction than does segregation of basaltic melt. Nevertheless, Laporte argued that melt fractions as low as 10% will segregate on time-scales of 10^5 yrs, whereas it had

been previously believed that melt fractions as high as 30% would not segregate on reasonable geologic time-scales.

7.6.6.3 Realistic models of mantle melting

As we pointed out above, in most circumstances melting in the mantle occurs because of decompression. (A possible exception is in subduction zones; here the generation of melt is still poorly understood, but may ultimately be due to hydration of the mantle wedge. Addition of water lowers the melting temperature, so this is a form of flux melting.) Decompression melting is necessarily a dynamic process: a parcel of mantle will begin to melt at some depth and will continue to melt as it rises. The fraction of melt produced will increase with height above the initial melting depth. If, as we have argued above, melt segregates readily, melt will rise faster than the solid. As a result, once the parcel of mantle has risen above the depth where melting begins, melt from below will continually stream through it. The melt entering the parcel from below will initially not be in equilibrium with the solid within the parcel, having been produced as a smaller melt fraction at greater depth (and hence greater pressure and temperature). Thus melt passing through the parcel will react with the solid in an attempt to reach equilibrium with it. This is similar to the process we described above as zone refining.

The situation then is analogous to diagenesis in sediments, which we discussed in Chapter 5. There are some differences, however. In diagenesis, the fraction of solid relative to fluid does not change, except through expulsion of fluid. In the melting process, solid is converted to fluid by nature of the process. In the melting process, length scales are such that diffusion does not significantly contribute to the flux and bioturbation does not exist, so advection is the only significant flux. Furthermore, our reduction of the problem to one dimension by assuming lateral uniformity will not be valid for the melting process. This is because the extent of melt will also decrease with distance from the some central point (a point under a volcano or under a spreading mid-ocean ridge), and because melt will be focused in from these peripheral regions toward the center. With these caveats, however, the diagenetic equation (eqn. 5.154) may be directly applicable to the melting process.

Unfortunately, a truly thorough quantitative treatment of the melting process has not yet been undertaken. In one of the more thorough discussions to date, Langmuir *et al.* (1993) concluded that despite the complexity of the melting process, the batch melting equation gives a reasonably good approximation of incompatible element concentrations in the melt as a function of the *average* degree of melting. Beneath mid-ocean ridges, the average degree of melting will be less than the maximum degree of melting, because different parcels of mantle follow different paths. Only mantle directly beneath the ridge is able to rise the maximum amount, and hence melt the maximum amount. In the simple case illustrated in Figure 7.28a, the average extent of melting is one half the maximum extent. Other ratios are possible for other models of mantle flow.

There are two situations where batch melting may not be a good approximation of incompatible element concentrations. The first is where there is a large volume of mantle from which only very low degree melts are extracted. This situation might arise as a result of suppression of the solidus by H_2O or CO_2 fluid, a well-established phenomenon. If melting is such that a small fraction of melt, say 0.1% or so, is generated between the "wet solidus" (i.e., H_2O or CO_2 present) and the "dry solidus" and the temperature range between the two is large, there could be a large region at great depth where very small degree melts are produced (Figure 7.28b). Mixing of these small degree melts with larger degree ones produced above the dry solidus then results in melt compositions different from those predicted by the batch melting equation (Plank and Langmuir, 1992). The second situation occurs when there is a phase change within the melting region. For example, spinel is replaced by garnet as the aluminous phase in the mantle at about 60–90 km depth. These two minerals have very different partition coefficients for some elements (Table 7.5), hence melts produced in the garnet stability region will have different incompatible element concentrations (and in particular, different rare earth patterns) than those in the spinel stability region.

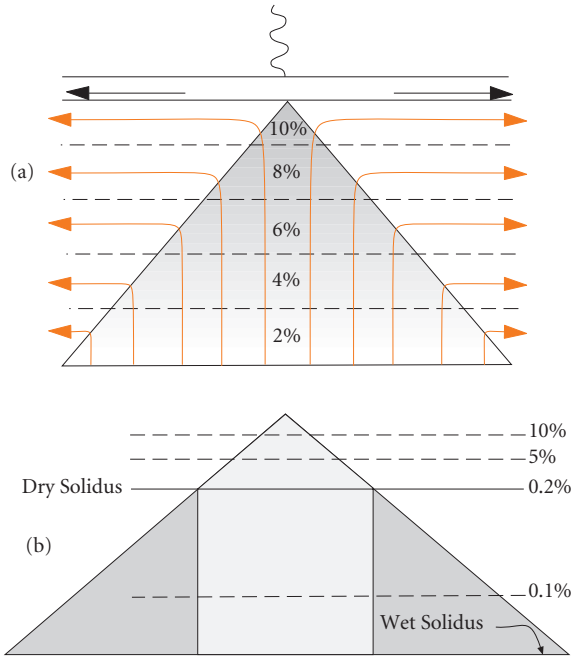

Figure 7.28 (a) Melting regime under a mid-ocean ridge. Red lines show the flow of mantle induced by passive spreading of overlying plates. Since melting results from decompression, no further melting occurs once motion becomes horizontal. Only those parts of the mantle directly under the ridge reach the maximum extent of melting. The melting regime along-ridge can be assumed to be uniform parallel to the ridge, hence the process is two-dimensional. The cartoon is, however, readily adapted to mantle-plume related volcanism by assuming radial symmetry. (b) Low-degree melts generated between the "wet" and "dry" solidi could enrich higher degree melts from the normal mantle column (light shading) in highly incompatible elements. However, the volume of this region must be large (typically 10 times that of the normal mantle column) for this to be effective, requiring efficient transport and focusing of melt over scales of hundreds of kilometers. Adapted from Plank and Langmuir (1992).

7.7 TRACE ELEMENT DISTRIBUTION DURING CRYSTALLIZATION

7.7.1 Equilibrium crystallization

Equilibrium crystallization occurs when the total liquid and total solid remain in equilibrium throughout the crystallization. If we define X as the fraction of material crystallized, then

$$\frac{C_i^l}{C_i^0} = \frac{1}{DX + (1 - X)} \tag{7.81}$$

where C^ℓ is the concentration in the remaining liquid and $C°$ is the concentration in the original liquid (we derive this equation in a manner exactly analogous to eqn. 7.42). The limit of trace element enrichment or depletion occurs when $X = 1$, when $C_l/C_o = 1/D$. Equilibrium crystallization requires the liquid keeps in contact with all crystals. Crystal interiors would have to maintain equilibrium through solid state diffusion, a slow process. Thus equilibrium crystallization is probably relevant only to a limited range of situations, such as the slow crystallization of an intrusion.

7.7.2 Fractional crystallization

Fractional crystallization, which assumes only instantaneous equilibrium between solid and liquid, is a more generally applicable model of crystallization. In this case, trace element concentrations in the melt are governed by:

$$\frac{C_i^\ell}{C_i^o} = (1 - X)^{D-1} \tag{7.82}$$

There is no limit to the enrichment or depletion of the liquid in this case. If D is very large, C^ℓ/C^o approaches 0 as X approaches 1, and it approaches ∞ as X approaches 1, if D is very small. What happens when $D = 0$?

For multiphase crystallization, we need to replace D in eqns. 7.81 and 7.82 with the bulk distribution coefficient as we defined it in eqn. 7.46, where m_ϕ in that equation would become the fraction of phase ϕ in the crystallizing mass.

Though fractional crystallization can, in principle, produce extreme trace element enrichment, this rarely occurs. A melt that has crystallized 90% or more (which would produce a ten-fold enrichment of a perfectly incompatible element in the melt) would have major element chemistry very different from its parent. From our knowledge of the compositional dependence of partition coefficients, we could predict that incompatible